

## Microstructural characterization of inhomogeneity in 9Cr ODS EUROFER steel

Das, A.; Chekhonin, P.; Altstadt, E.; Bergner, F.; Heintze, C.; Lindau, R.;

Originally published:

May 2020

**Journal of Nuclear Materials 533(2020), 152083**

DOI: <https://doi.org/10.1016/j.jnucmat.2020.152083>

Perma-Link to Publication Repository of HZDR:

<https://www.hzdr.de/publications/Publ-29964>

Release of the secondary publication  
on the basis of the German Copyright Law § 38 Section 4.

CC BY-NC-ND

# Microstructural characterization of inhomogeneity in 9Cr ODS EUROFER steel

A. Das<sup>1,a</sup>, P. Chekhonin<sup>a</sup>, E. Altstadt<sup>a</sup>, F. Bergner<sup>a</sup>, C. Heintze<sup>a</sup>, R. Lindau<sup>b</sup>

<sup>a</sup> Helmholtz-Zentrum Dresden-Rossendorf, Bautzner Landstrasse 400, 01328 Dresden (Germany)

<sup>b</sup> Institute for Applied Materials, Karlsruhe Institute of Technology, Hermann-von-Helmholtz-Platz 1, 76344 Eggenstein-Leopoldshafen, Germany

<sup>1)</sup> Corresponding author, e-mail: a.das@hzdr.de

## Abstract

Ferritic-martensitic ODS steels are one of the candidate materials for Gen-IV nuclear fission and fusion reactors. Residual ferrite was often found in the microstructure of 9Cr ODS steels. This constituent was reported to be responsible for the superior creep and high-temperature strength. Using optical microscopy of an air-cooled batch of ODS EUROFER, inhomogeneous regions in the microstructure have been found with similar appearance to previously reported residual ferrite. In order to avoid a potential misinterpretation of inhomogeneous regions as residual ferrite, detailed microstructural investigations have been carried out on the inhomogeneous regions using site-specific nanoindentation, scanning electron microscopy including electron backscatter diffraction, and transmission electron microscopy. It is demonstrated that the inhomogeneous regions are free of oxide nanoparticles, which possibly form due to imperfect mechanical alloying. These regions also exhibit lower hardness which is attributed to the absence of nanoparticles and a lower dislocation density. It is concluded that optical microscopy alone is insufficient to distinguish beneficial residual ferrite from undesired particle-free regions. Our findings are underpinned by the consistency between the calculated theoretical yield strength, the yield strength converted from the indentation hardness and the yield strength obtained from tensile testing.

## Keywords

ODS steel, ferritic-martensitic steel, inhomogeneity, nanoindentation, residual ferrite

## Highlights

- Inhomogeneous regions of an air-cooled batch of ODS EUROFER were investigated using electron microscopy and site-specific nanoindentation
- Inhomogeneous regions are not residual ferrite as they exhibit lower hardness than the matrix and contain no oxide nanoparticles
- The absence of nanoparticles and a lower dislocation density are mainly responsible for the lower hardness of the inhomogeneous regions
- Optical microscopy alone is insufficient to identify inhomogeneous regions as being residual ferrite
- Reasonable consistency in the yield strength obtained from different methods is achieved

## 1 Introduction

Among ODS steels, which are candidate materials for use as cladding tubes in Gen-IV nuclear fission reactors and as blankets for fusion reactors, two classes draw major attention. The first is the 9-12 wt.% Cr ferritic-martensitic variant of ODS steels and the second is the 12-20 wt.% Cr ferritic variant. With respect to the first class, active research has been conducted in the US [1–3] and in Japan [4–10]. In Europe, ODS EUROFER, a reduced-activation ferritic-martensitic (RAFM) 9% Cr ODS steel, was developed as a candidate material for advanced breeding blankets in fusion reactors. Several versions of ODS EUROFER were produced as a result of systematic development of RAFM steels in Europe [11]. One of these versions is the air-cooled EU batch of ODS EUROFER which is investigated in the present work.

Residual  $\alpha$ -ferrite, the phase which remains untransformed during austenitization, was often reported in the microstructure of 9% Cr ODS steels [4,9,10,12–15]. Residual ferrite is frequently identified as bright, smooth and sometimes elongated regions in a dark matrix using optical microscopy (OM) [4,8,10,13–19]. Residual ferrite contains a high number density of oxide nanoparticles, which are even smaller than the nanoparticles in the tempered martensite matrix. Residual ferrite phase is reported to be responsible for providing superior creep and high-temperature strength to ferritic-martensitic ODS steels [4,13,20–22]. The amount of residual ferrite in the microstructure can be controlled by varying the amounts of Ti, Cr, W, C,  $Y_2O_3$  and excess O in the material [8,10,13,15,17,23]. Improvements in creep and high-temperature strength of 9% Cr ODS steels have been achieved by careful control of the composition.

Recently, Fu et al. found similar looking bright regions by optical microscopy in ODS EUROFER and reported them as residual ferrite [16]. Contrary to this, Lucon et al. for a batch of ODS EUROFER suspected such bright regions to be zones which were not mechanically alloyed with  $Y_2O_3$  [24]. However, in references [16], [24] and other publications, detailed microstructural investigations were not undertaken to ascertain the nature of these inhomogeneities.

The present study focusses on avoiding a potential misinterpretation of inhomogeneous regions as residual ferrite due to their similar appearance under the optical microscope. It has been shown that residual ferrite phase is important for the creep strength of ferritic martensitic ODS steels. Therefore, the presence or absence of residual ferrite phase along with its correct interpretation is important as it affects the mechanical properties. In this work besides OM, scanning electron microscopy (SEM), electron backscatter diffraction (EBSD), transmission electron microscopy (TEM) and site-specific nanoindentation are combined to facilitate a clear distinction. In order to check the consistency of these observations, the yield strength converted from the indentation hardness is compared with both the yield strength directly measured by tensile testing and the theoretical yield strength calculated on the basis of microstructure-informed strengthening contributions.

## 2 Materials and methods

### 2.1 Material

The European reference RAFM steel is denominated as EUROFER; its nominal composition (in wt.%) is 8.9Cr, 1.1W, 0.2V, 0.14Ta, 0.42Mn, 0.06 Si, 0.11 C and Fe for the balance [25].

The air-cooled EU batch of ODS EUROFER was prepared in order to optimize the creep strength and fracture toughness. The production route involved mechanical alloying (MA) of steel powder with 0.3 wt.% Y<sub>2</sub>O<sub>3</sub> followed by compaction using hot isostatic pressing (HIP). After this, the material was thermo-mechanically treated including hot-rolling (HR) at 1150 °C and then cooling to room temperature (RT) followed by re-austenitization at 1100 °C for 30 min with air-cooling to RT and tempering at 750 °C for 2 h. Even though the material was not water quenched, the cooling rate after austenitization was still high enough for martensite formation. The composition of the air-cooled EU batch is presented in Table 1. Tensile testing of samples with gauge length parallel to the rolling direction indicated a yield strength of 886 MPa at room temperature.

Table 1 Composition of the air-cooled EU batch of ODS EUROFER in wt%

| Cr  | W    | V    | Ta   | Mn   | Si   | C     | Ti     | Fe   | Y <sub>2</sub> O <sub>3</sub> |
|-----|------|------|------|------|------|-------|--------|------|-------------------------------|
| 9.2 | 1.14 | 0.19 | 0.03 | 0.38 | 0.03 | 0.086 | 0.0003 | 88.5 | 0.312                         |

## 2.2 Microscopy

Optical microscopy (Leica REICHERT MEF4) was used to investigate the bulk microstructure. The samples were etched for 10 minutes using picric acid with ammonia washout. For SEM investigation, the sample were etched using 50 ml distilled water, 15 ml hydrochloric acid and 2.5 g iron (III) chloride. The purpose of the etching was to highlight the carbides and the grain boundaries. A Zeiss EVO 50 SEM equipped with a tungsten electron cathode was used for secondary electron (SE) and back scatter electron (BSE) contrast imaging.

To obtain information about the grain distribution, EBSD was applied in a Zeiss NVision 40 CrossBeam (SEM and focused ion beam (FIB)) equipped with a field emission electron cathode (FEG) and a Bruker EBSD acquisition system including an e- Flash HR+ detector. Sample preparation for SEM and EBSD consisted of grinding and (as the last step) of mechanical polishing using an oxide polishing suspension (OP-S) consisting of amorphous silica, water and 1,3-butanediol. For all EBSD measurements an acceleration voltage of 15 kV and a step size of 0.08 μm were used.

In addition to the Bruker EBSD software, an in-house written EBSD evaluation software was applied for the correction of unindexed points, determination of grain boundaries and to plot internal misorientation (for any measured pixel) with respect to the corresponding average grain orientation. The minimum misorientation angle for the grain reconstruction was arbitrarily fixed at 10°. Only grains consisting of 5 or more than 5 mapping pixels (≡ equivalent diameter of 0.2 μm) were considered in the evaluation.

TEM investigations were performed using a Talos F200X FEG-(S) TEM (FEI) operated at 200 keV to obtain details on the included particles. Samples were prepared by means of electro-polishing in a TenuPol-5 (Struers) in 5% perchloric acid in methanol at -60 °C applying a voltage of 23 V. Additionally, in order to clarify local inhomogeneities, a TEM lamella was prepared by FIB using the above-mentioned Zeiss CrossBeam FIB system. Scanning transmission electron microscope (STEM) micrographs and diffraction patterns using selected area diffraction (SAD) of grains which were oriented with the beam direction parallel to <001> were recorded.

## 2.3 Nanoindentation

The microstructure was analysed using site-specific nanoindentation in order to investigate the inhomogeneous regions. Nanoindentation testing was performed using the Universal Nanomechanical Tester (UNAT, Advanced Surface Mechanics GmbH, now Zwick GmbH) equipped with a Berkovich indenter. Indentation loads in the range from 1 to 50 mN were applied. The measuring cycle consisted of loading for 250 s, a creep segment for 20 s, an unloading segment for 8 s, a holding segment for 60 s and a final unloading segment of 1.6 s. The calibration of the indenter area function and the instrument stiffness was based on measurements on two reference materials (fused silica, sapphire) with known elastic moduli. Data correction included zero point correction which was done assuming Hertzian contact for the first several 10 nm of the loading curve.

A thermal drift correction was not necessary due to the short duration of the measuring cycle. Additionally, the system was equipped with thermal insulation and allowed to equilibrate for at least 45 min prior to the measurements. Data analysis was done by means of a method developed by Doerner and Nix [26] and improved and adapted to pyramidal indenters by Oliver and Pharr [27,28].

## 3 Results

### 3.1 Characterization of the bright stripes

Optical microscopy on etched samples of the air-cooled EU batch of ODS EUROFER reveals some inhomogeneous regions which appear as “bright stripes” elongated along L (rolling direction RD) and T (transverse direction TD). These are marked with dashed white ellipses in Fig. 1. Their thickness (along S, normal direction ND) ranges from a few  $\mu\text{m}$  up to 10  $\mu\text{m}$ . The area fraction of the bright stripes is roughly estimated to be approximately 4%. It is interesting to note that, for a random two-phase microstructure, the area fraction coincides with the volume fraction. However, the present arrangement of the bright stripes deviates from randomness, meaning that the volume fraction may deviate from 4%. The rest of the microstructure appears homogenous in optical microscopy with many dark spots. These dark spots are identified as areas around pre-dominantly Cr, W and C rich precipitates of the  $\text{M}_{23}\text{C}_6$  type. These carbides are preferably located at grain boundaries with an average size of 0.23  $\mu\text{m}$  and a number density of  $8.3 \times 10^{18} \text{ m}^{-3}$ . Additionally, SEM BSE contrast images indicate lower carbide number density within the bright stripes as compared to the matrix resulting in slightly darker appearance in the BSE contrast of the SEM (Fig. 2).

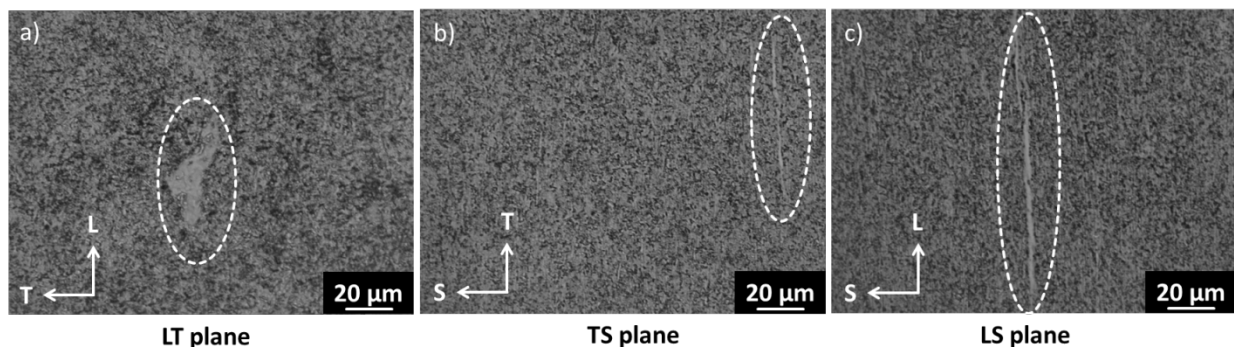


Fig. 1 The microstructure of the etched air-cooled EU batch of ODS EUROFER using optical microscopy. The bright stripes (inside dashed ellipses) seem to be elongated in the L and the T directions.

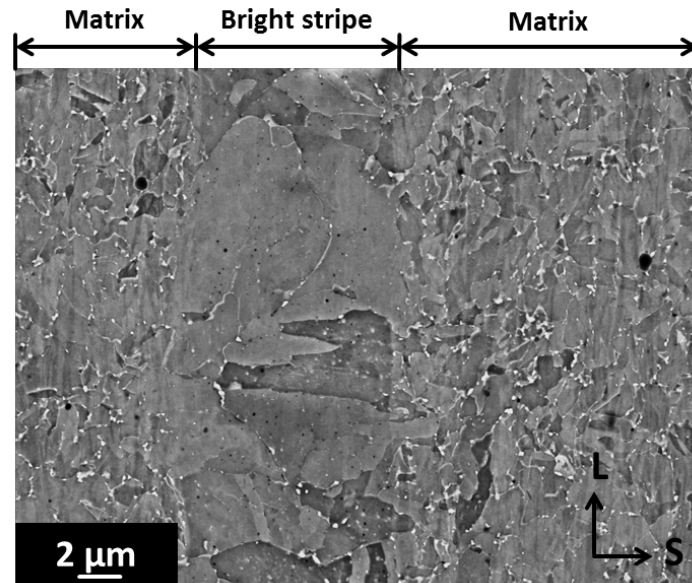


Fig. 2 A BSE contrast image with a bright stripe and adjoining matrix regions. The carbides appear bright and prefer grain boundaries. The number density of carbides is less inside the bright stripes as compared to the matrix.

EBSB reveals high angle grain boundaries (HAGBs) inside these bright stripes belonging to coarser grains in comparison to the surrounding matrix (Fig. 3). Applying the line intercept method locally, the average grain size in the bright stripe is measured to be about 1.7 μm while the average grain size in the matrix is 0.9 μm. Most of the grains inside and outside these bright stripes exhibit a noteworthy internal misorientation as can be seen from Fig. 3c.

FIB was used to cut a lamella which included both the bright stripe and the matrix region (Fig. 4a and b). As demonstrated by STEM, nanoparticles in the size range of 10 nm or below were not observed in the bright stripe region (Fig. 4c, Fig. 5d and Fig. 5e) while the matrix region exhibited many nanoparticles (Fig. 4d, Fig. 5a and Fig. 5b). For both, the matrix and the bright stripe region, the corresponding selected area diffraction (SAD) patterns do not present any additional reflexes (Fig. 5c and f). Due to their small size and their small volume fraction, the nanoparticles do not contribute to the SAD pattern. This was previously observed by Ribis et al. [29]. Additionally, by comparing Fig. 5a and Fig. 5d, it is obvious that the dislocation density is much lower in the bright stripe region. The flecks observed in the bright stripe region are artefacts caused by the FIB preparation and not nanoparticles, as was confirmed by local energy dispersive x-ray spectroscopy measurements (not shown here).

Small angle neutron scattering (SANS) of the bulk microstructure has already been performed on the air-cooled EU batch of ODS EUROFER [30]. The nanoparticles exhibit a crystalline structure of almost spherical shape and are enriched in Y and O in the ratio 2:3 with minor amounts of Fe, Cr and Si [30]. The average diameter of the nanoparticles is 3.8 nm with a number density of  $11.5 \times 10^{22} \text{ m}^{-3}$ .

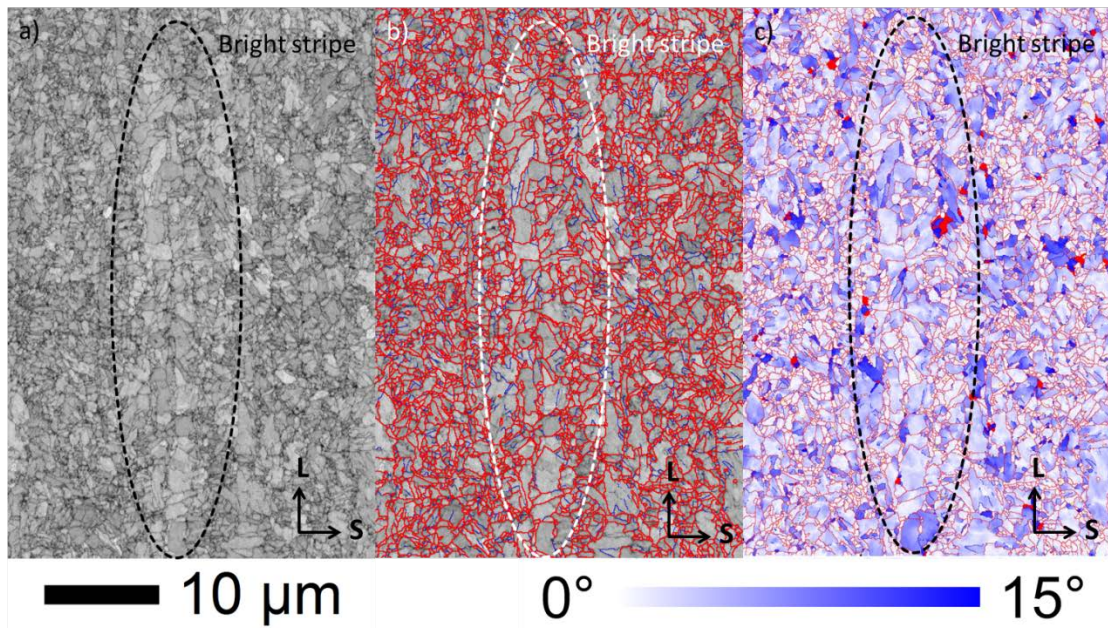


Fig. 3 a) EBSD pattern quality map of the air-cooled EU batch of ODS EUROFER highlighting a bright stripe, b) Grain boundary map showing HAGB (grain boundary misorientation angle  $\geq 15^\circ$ ) as red lines and low angle grain boundaries (grain boundary misorientation angle between  $5^\circ$  and  $15^\circ$ ) as blue lines and c) Internal misorientation (for any measured pixel) with respect to the corresponding average grain orientation: white colour for zero, fading to blue with increasing internal misorientation. Points exceeding  $15^\circ$  internal misorientation are coloured red. HAGBs and low angle grain boundaries (LAGBs) are coloured blue and red, respectively.

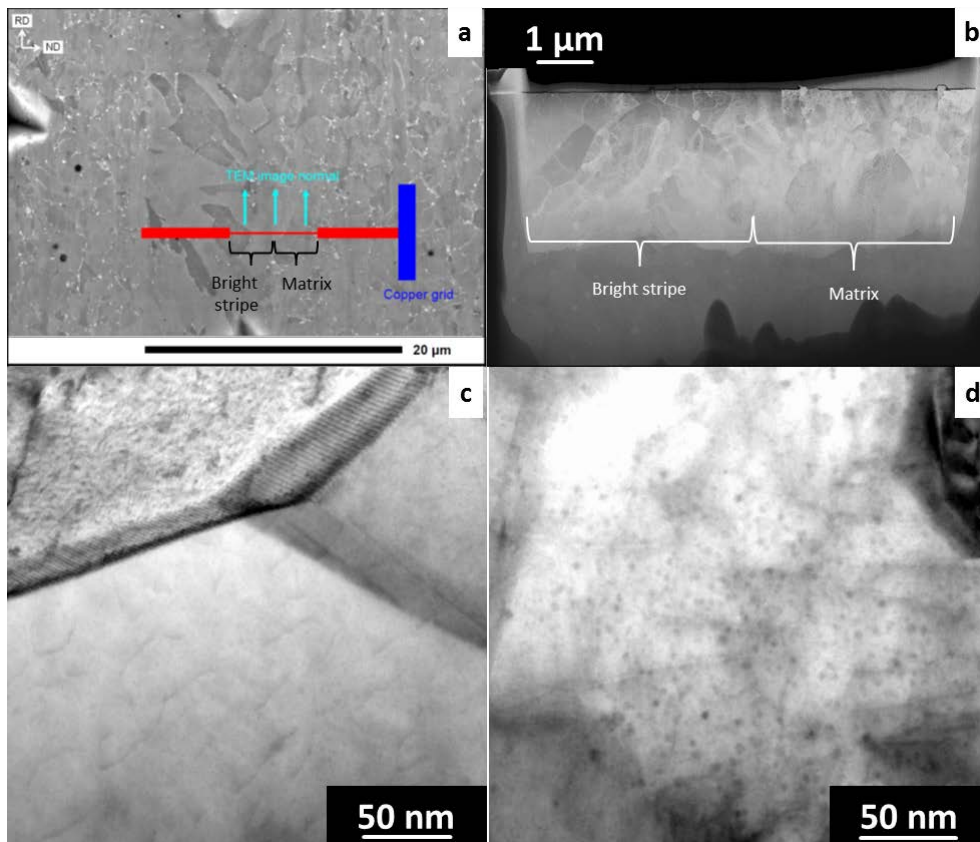


Fig. 4 a) A SEM micrograph showing the FIB lamella taken out from the etched air-cooled EU batch of ODS EUROFER including areas from a bright stripe and the adjoining matrix region, b) a STEM dark field image of the lamella including both the regions, c) a STEM bright field image from the bright stripe region and d) a STEM bright field image from the matrix region

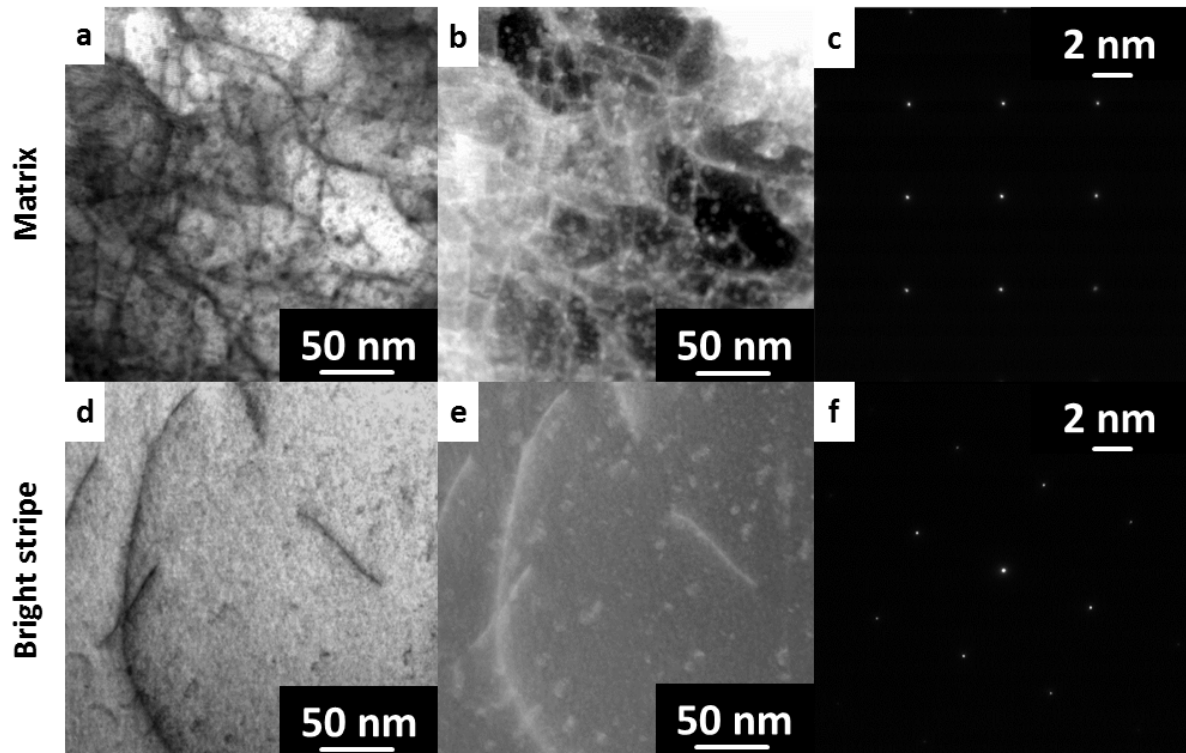


Fig. 5 Matrix region: a) STEM bright field image, b) STEM dark field image and c) selected area diffraction (SAD) pattern from the same grain. Electron beam is parallel to  $\langle 001 \rangle$  direction. Bright stripe region: d) STEM bright field image, e) STEM dark field image and f) SAD pattern from the same grain. Electron beam is parallel to  $\langle 001 \rangle$  direction. The little flecks in d) and e) are artefacts caused by the FIB sample preparation.

### 3.2 Nanoindentation

Nanoindentation was performed on two different bright stripes (with respect to optical microscope images) on the LS plane and also on two different adjoining matrix regions (darker regions in optical micrographs) of the air-cooled EU batch of ODS EUROFER. An OM and a BSE SEM image are presented in Fig. 6 for one of these bright stripes after nanoindentation. An average load displacement curve is calculated from the single corrected curves of more than 8 indents in the matrix and more than 4 indents in the bright stripe which were placed in a regular array with a spacing of  $30 \mu\text{m}$  to avoid interference by neighbouring indents. To calculate the average curve, the load or holding time in case of the holding segment, is divided into intervals. The data points of all curves within this interval are averaged. The standard deviation of load and displacement is calculated for each interval and used for the calculation of the statistic errors in the subsequent analysis.

A reference depth of 400 nm was chosen in order to eliminate the uncertainties associated with low load measurements [31] and also to not exceed the thickness of the bright stripe. The average indentation hardness values measured at the reference depth of 400 nm for the matrix is  $4.28 \pm 0.26 \text{ GPa}$  while it is  $2.82 \pm 0.29 \text{ GPa}$  for the bright stripes. Clearly, the bright stripes are softer than the matrix.

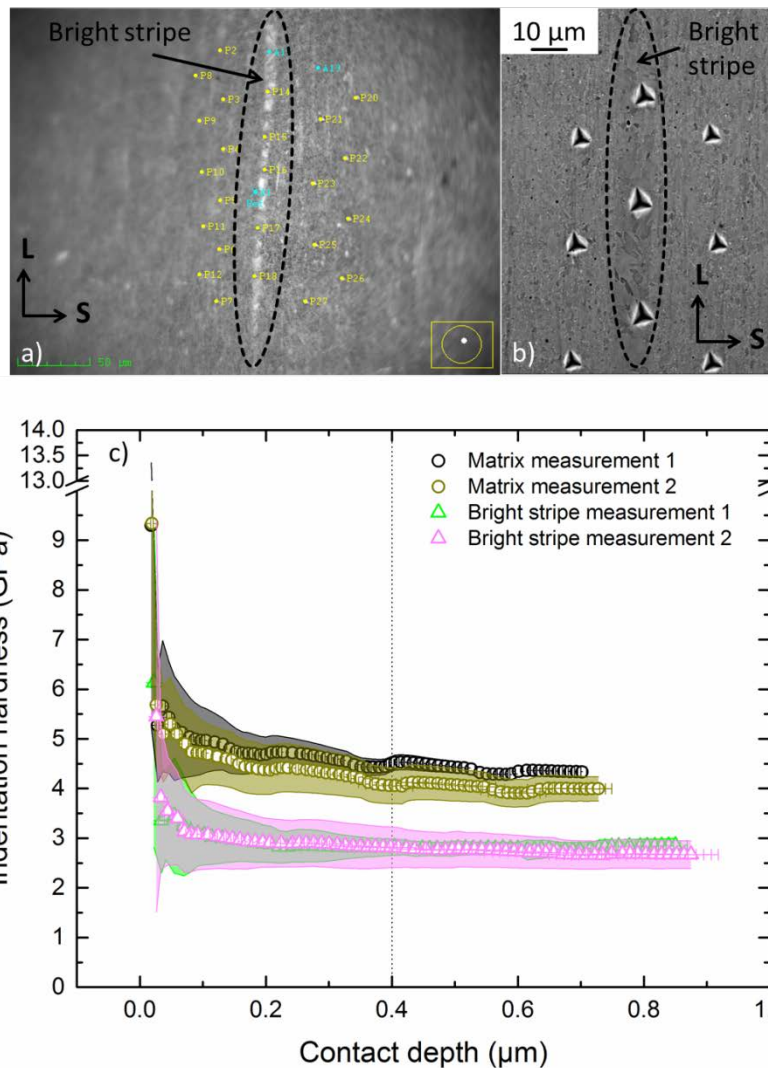


Fig. 6 The nanoindented region including the bright stripe and the matrix using a) OM, b) SEM BSE mode and c) a graph indicating indentation hardness as a function of contact depth

## 4 Discussion

In this section, we discuss about the appearance, origin, microstructure and the indentation hardness of the inhomogeneous regions (bright stripes). Values from indentation hardness testing are also compared with values from conventional tensile testing and a theoretical yield strength model based on strengthening mechanisms.

### 4.1 Investigation of the bright stripes

The reason, why the stripes appear bright, is believed to be due to the lower number density of carbides in these regions and to the resulting etching behaviour.

#### 4.1.1 Comparison with residual ferrite

The bright stripes in the optical micrographs (Fig. 1) look similar to the residual  $\alpha$ -ferrite phase which forms during the incomplete reverse transformation of  $\alpha$ -ferrite to  $\gamma$ -austenite during the austenitization at 1100 °C step due to the blocking of  $\alpha$ -ferrite/ $\gamma$ -austenite interfaces by nanoparticles in the matrix [4,8,10,13–19]. Some researchers also report the

presence of  $\delta$ -ferrite which forms at temperatures close to 1200 °C [32]. However, in the present work,  $\delta$ -ferrite can be ruled out due to lower austenitization temperature.

The following arguments prove that the bright stripes in the microstructure of the air-cooled EU batch of ODS EUROFER are not residual ferrite:

### **Internal misorientation**

If the bright stripes comprised only of a purely ferrite phase, then it would be expected that these regions contained grains without any internal misorientation. A rather globular grain shape would also be expected assuming the ferrite forms by a reconstructive transformation (diffusion of iron atoms) [33]. However, in the present work, EBSD reveals grains inside the bright stripes exhibiting a noteworthy internal misorientation and are coarser in comparison to its surrounding matrix (Fig. 3). The grains are also slightly elongated and non-globular which indicates that these bright stripes underwent a martensitic transformation at some stage during its thermo-mechanical treatment history. The microstructure essentially is tempered martensitic.

### **Oxide nanoparticles**

The residual ferrite phase exhibits a high number density of fine oxide nanoparticles [4,7,9,13,22,34]. However, the bright stripes in the air-cooled EU batch of ODS EUROFER do not exhibit any nanoparticles in contrast to the surrounding matrix regions as can be seen from the TEM micrographs (Fig. 4c, d and Fig. 5). The rolling process resulted in a plaque shape of the particle-free zones in the L-T plane, thus forming stripes in the L-S and T-S planes (Fig. 1). The absence of nanoparticles enhances the grain and phase boundary mobility leading to a larger grain size in the austenitization process. A larger grain size is equivalent to a smaller grain boundary length per unit volume and, consequently, to a lower number density of grain boundary carbides (Fig. 2).

### **Hardness**

Residual  $\alpha$ -ferrite is known to exhibit higher hardness than tempered martensite due to the presence of a higher number density of finer oxide nanoparticles, which obstruct dislocation motion [4,8,22,34]. However, the bright stripes in the air-cooled EU batch of ODS EUROFER exhibit lower indentation hardness than the matrix as demonstrated in Fig. 6. This is consistent with the absence of oxide nanoparticles observed by TEM and, therefore, confirms the interpretation of the bright stripes as particle-free regions instead of residual ferrite.

### **Composition**

Many ODS steels which reported the presence of residual ferrite contained higher contents of ferrite stabilizers such as Ti, Cr and W [13,15,17,23] as compared with the air-cooled EU batch of ODS EUROFER. They also contained slightly higher  $Y_2O_3$  content which results in higher residual ferrite formation [10]. A decrease in C content leading to a higher residual ferrite phase was reported in [8] while a high excess O content (> 0.11 wt.%) was reported to have a detrimental effect on the creep and high-temperature strength by reduction of the residual ferrite phase [15].

In comparison, the air-cooled EU batch of ODS EUROFER contains lower W, C,  $Y_2O_3$  and a negligible amount of Ti (Table 1). This contributes to the absence of the residual ferrite phase. The lower amount of C is able to provide enough driving force for the reverse

transformation of  $\alpha$ -ferrite to  $\gamma$ -austenite as most of the C remains in the solution without strong combiners such as Ti in the material.

#### 4.1.2 Comparison with retained austenite

Retained austenite phase was reported in the microstructure by Zilnyk et al. for a similarly manufactured ODS EUROFER [35]. The suspicion that the bright stripes can be retained austenite phase is eliminated, as the applied EBSD system can distinguish between bcc and fcc phases. No fcc steel phase was detected in the microstructure.

#### 4.1.3 Formation postulation

Bright stripes are most probably formed due to improper mechanical alloying. Similar findings were reported by Lucon et al. [24]. During the thermomechanical treatment procedures, recrystallization takes place and may change the distribution of the oxide particles. However, two arguments lead to the conclusion that recrystallization is likely not responsible for the existence of bright stripes:

1. Shape of the bright stripes: Generally, recrystallization would include grain boundary migration in all directions leading to rather globular or only slightly elongated particle-free zones. However, the shape of the presently observed particle-free zones has a very high aspect ratio (typically  $\gg 2$ ). Therefore, their pan-cake shape (Fig. 1) must have been finally influenced by the geometry of the rolling process and remained unaffected by dynamic recrystallization during HR and the following re-austenization.
2. Size of the particle-free zones: Particle-free zones of thickness close to 100 nm are expected when they are formed due to a moving grain boundary [36]. However, in the present work, particle-free zones of thickness an order of magnitude higher have been found.

## 4.2 Yield strength estimation of different regions

This section aims to check the consistency between values of the yield strength based on direct measurement (tensile test), converted from nanohardness measurements, and calculated on the basis of strengthening mechanisms.

### 4.2.1 Hardness-converted yield strength and comparison with tensile testing

The indentation hardness  $H_{IT}$  measured at a reference depth of 400 nm has been converted into yield strength  $\sigma_{y,IT}$  using Eq. 1 (units of GPa) [37].

$$\sigma_{y,IT} = 0.44 (H_{IT} - 1.96) \quad (1)$$

The indentation hardness values for the bright stripes and matrix were both averaged from the available results given in section 3.2. The yield strengths converted according to Eq. 1 are presented in Table 2 and compared with the yield strength of the bulk material obtained by conventional tensile testing. As expected, the bulk value lies between the values representing the two components (bright stripes and matrix) of the material and is closer to the value obtained for the matrix. This is consistent with the fact that the volume fraction of the bulk material is dominated by the matrix.

Table 2 The yield strength of the individual components of air-cooled EU batch of ODS EUROFER in comparison with the yield strength of bulk materials

| Material/region                                 | Type of measurement         | Yield strength (MPa) |
|---|-----------------------------|----------------------|
| Bright-stripe region of ODS EUROFER (this work) | Converted from nanohardness | 378 ± 126            |
| Matrix region of ODS EUROFER (this work)        | Converted from nanohardness | 1021 ± 113           |
| Air-cooled batch of ODS EUROFER (this work)     | Tensile test                | 886                  |
| EUROFER-97 [38]                                 | Tensile test                | 520                  |

The hardness-converted yield strength obtained for the bright stripes, which were found to be free of nanoparticles, can be compared with the yield strength reported for a suitable non-ODS material. EUROFER-97, having the same basic composition, is a candidate material for this kind of comparison. The yield strength at room temperature reported for EUROFER-97 is provided in Table 2 [38]. Consistent with our expectation, this value is not far from the value observed for the bright stripes.

#### 4.2.2 Theoretical yield strength and comparison with hardness-converted yield strength

The theoretical yield strengths representative of bright stripes and matrix were calculated using the empirical strengthening model by Chauhan et al., Eq. 2 [39].

$$\sigma_{y,th} = \sigma_g + \sqrt{\sigma_d^2 + \sigma_p^2} \quad (2)$$

Here,  $\sigma_{y,th}$  is the theoretical yield strength and  $\sigma_g$ ,  $\sigma_d$  and  $\sigma_p$  are contributions from Hall-Petch strengthening, dislocation forest strengthening and nanoparticle strengthening, respectively. It is important to note that the number density of carbides is roughly four orders of magnitude less than the number density of oxide nanoparticles, meaning that the strengthening contribution of carbides can be ignored in  $\sigma_p$ , and consequently in Eq. 2 as compared with the strengthening contribution from nanoparticles. The formulas and constants used to calculate the strengthening contributions are those reported in [39] to properly reflect the behaviour of a number of ODS and non-ODS Fe-Cr alloys including ODS EUROFER. Appropriate values of the grain size, the diameter and number density of nanoparticles, and the dislocation density are presented in Table 3 for the bright stripes and the matrix along with the calculated contributions to the theoretical yield strength. The total yield strength according to Eq. 2 and the yield strength converted from indentation hardness are compared in this table. Nanoparticle strengthening is assumed to be negligible in the bright stripes where no nanoparticles were observed.

Table 3 Hardness-converted ( $\sigma_{y,IT}$ ) and theoretical yield strengths ( $\sigma_{y,th}$ ) with contributions from Hall-Petch strengthening ( $\sigma_g$ ), nanoparticle strengthening ( $\sigma_p$ ) and dislocation forest strengthening ( $\sigma_d$ )

| Region               | Grain size ( $\mu\text{m}$ ) | $\sigma_g$ (MPa) | Nano-particle size (nm) | Number density ( $10^{22} \text{ m}^{-3}$ ) | $\sigma_p$ (MPa) | Dislocation density ( $10^{14} \text{ m}^{-2}$ ) | $\sigma_d$ (MPa) | $\sigma_{y,th}$ (MPa) | $\sigma_{y,IT}$ (MPa) |
|----------------------|------------------------------|------------------|-------------------------|---|------------------|--|------------------|-----------------------|-----------------------|
| Bright stripes       | 1.7<br>(this work)           | 205              | 0                       | 0   | 0                | 7<br>[39,40]                                     | 569              | 774                   | 370                   |
| Bright stripes (mod) |                              |                  |                         |   |                  | 0.7<br>(assumed)                                 | 180              | 385                   |                       |
| Matrix               | 0.9<br>(this work)           | 282              | 3.8<br>[30]             | 11.5<br>[30]                                | 449              | 7<br>[39,40]                                     | 569              | 1007                  | 1030                  |

As the results in Table 3 demonstrate, the calculated theoretical yield strength and the hardness-converted yield strength reasonably agree for the matrix. This confirms the applicability of the applied procedure. For the bright stripes, the calculated theoretical yield strength is smaller than the theoretical yield strength of the matrix, which is understandable due to the missing strengthening contribution from nanoparticles, but still essentially larger than the hardness-converted yield strength. The one and only candidate to explain the latter discrepancy is the dislocation density in the bright stripe region. Indeed, during tempering the lack of pinning by nanoparticles presumably leads to stronger recovery as compared to the matrix region resulting in a lower dislocation density as compared to the matrix. This is in agreement with our STEM investigations (Fig. 5). If we assume a dislocation density of the bright stripe regions as one tenth of the matrix (Bright stripes (mod) in Table 3), similar theoretical and hardness-converted yield strengths are obtained. Consequently, both the lack of nanoparticles and a lower dislocation density are significantly contributing to the reduced yield strength of the bright stripes.

## 5 Conclusions

Inhomogeneous regions in the microstructure of an air-cooled EU batch of ODS EUROFER were characterized using electron microscopy and site-specific nanoindentation. Although the inhomogeneous regions, in the form of bright stripes, in the air-cooled EU batch of ODS EUROFER look similar to residual ferrite when using optical microscopy, evidence is provided that these regions are not residual ferrite in the present case. In fact, bright stripes are formed due to imperfect mechanical alloying resulting in the absence of nanoparticles in certain regions. This gives rise to higher grain boundary mobility, larger grain size and a lower number density of grain boundary carbides, which finally is believed to result in the distinct etching behaviour as observed by optical microscopy. It was demonstrated that optical microscopy alone is insufficient to identify bright stripes as residual ferrite and additional investigations using SEM, EBSD and TEM are needed. An extension of the MA period during manufacturing should lead to a homogenous microstructure [41], eliminating particle-free regions which are not expected to contribute to the creep and high temperature strength of ODS steels.

The conclusion drawn above is consistent with the observations based on nanoindentation indicating that bright stripes are significantly weaker than the matrix. The consideration of microstructure-informed strengthening contributions shows that this is mainly due to both the absence of nanoparticles and a lower dislocation density in the bright stripes. For both the bright stripes and the matrix, a reasonable agreement is found between the calculated theoretical yield strength, the yield strength converted from indentation hardness and the yield strength obtained from tensile tests of bulk materials.

## Acknowledgements

This work contributes to the Joint Programme on Nuclear Materials (JPNM) within the European Energy Research Alliance (EERA). The authors would like to thank Ms. Michaela Rossner for metallographic preparations, Ms. Annette Kunz for the FIB preparation and Mr. Wolfgang Webersinke for nanoindentation measurements. The chemical analysis of the bulk material was performed by Dr. Thomas Bergfeld, head of chemical analysis group in the department IAM-AWP of KIT.

## Data Availability

The raw/processed data required to reproduce these findings cannot be shared at this time as the data also forms part of an ongoing study.

## References

- [1] T.S. Byun, J.H. Yoon, S.H. Wee, D.T. Hoelzer, S.A. Maloy, Fracture behavior of 9Cr nanostructured ferritic alloy with improved fracture toughness, *J. Nucl. Mater.* 449 (2014) 39–48. <https://doi.org/10.1016/j.jnucmat.2014.03.007>.
- [2] T.S. Byun, J.H. Yoon, D.T. Hoelzer, Y.B. Lee, S.H. Kang, S.A. Maloy, Process development for 9Cr nanostructured ferritic alloy (NFA) with high fracture toughness, *J. Nucl. Mater.* 449 (2014) 290–299. <https://doi.org/10.1016/j.jnucmat.2013.10.007>.
- [3] T.S. Byun, D.T. Hoelzer, J.H. Kim, S.A. Maloy, A comparative assessment of the fracture toughness behavior of ferritic-martensitic steels and nanostructured ferritic alloys, *J. Nucl. Mater.* 484 (2017) 157–167. <https://doi.org/10.1016/j.jnucmat.2016.12.004>.
- [4] S. Ukai, S. Ohtsuka, T. Kaito, H. Sakasegawa, N. Chikata, S. Hayashi, S. Ohnuki, High-temperature strength characterization of advanced 9Cr-ODS ferritic steels, *Mater. Sci. Eng. A*. 510-511 (2009) 115–120. <https://doi.org/10.1016/j.msea.2008.04.126>.
- [5] S. Ukai, S. Mizuta, M. Fujiwara, T. Okuda, T. Kobayashi, Development of 9Cr-ODS martensitic steel claddings for fuel pins by means of ferrite to austenite phase transformation, *J. Nucl. Sci. Technol.* 39 (2002) 778–788. <https://doi.org/10.1080/18811248.2002.9715260>.
- [6] S. Ohtsuka, S. Ukai, M. Fujiwara, Nano-mesoscopic structural control in 9CrODS ferritic/martensitic steels, *J. Nucl. Mater.* 351 (2006) 241–246. <https://doi.org/10.1016/j.jnucmat.2006.02.006>.
- [7] H. Oka, T. Tanno, S. Ohtsuka, Y. Yano, T. Uwaba, T. Kaito, M. Ohnuma, Effect of thermo-mechanical treatments on nano-structure of 9Cr-ODS steel, *Nucl. Mater. Energy*. 9 (2016) 346–352. <https://doi.org/10.1016/j.nme.2016.10.007>.

- [8] R. Miyata, S. Ukai, X. Wu, N. Oono, S. Hayashi, S. Ohtsuka, T. Kaito, Strength correlation with residual ferrite fraction in 9CrODS ferritic steel, *J. Nucl. Mater.* 442 (2013) S138–S141. <https://doi.org/10.1016/j.jnucmat.2013.04.086>.
- [9] M. Yamamoto, S. Ukai, S. Hayashi, T. Kaito, S. Ohtsuka, Reverse phase transformation from  $\alpha$  to  $\gamma$  in 9Cr-ODS ferritic steels, *J. Nucl. Mater.* 417 (2011) 237–240. <https://doi.org/10.1016/j.jnucmat.2010.12.250>.
- [10] M. Yamamoto, S. Ukai, S. Hayashi, T. Kaito, S. Ohtsuka, Formation of residual ferrite in 9Cr-ODS ferritic steels, *Mater. Sci. Eng. A.* 527 (2010) 4418–4423. <https://doi.org/10.1016/j.msea.2010.03.079>.
- [11] E. Lucon, Tensile and fracture toughness properties of EUROFER ODS (“EU Batch”-6mm Plate) in the unirradiated condition, SCK·CEN Open Rep. BLG-1024. (2006). <http://publications.sckcen.be/dspace/handle/10038/230>.
- [12] C. Cayron, E. Rath, I. Chu, S. Launois, Microstructural evolution of Y<sub>2</sub>O<sub>3</sub> and MgAl<sub>2</sub>O<sub>4</sub> ODS EUROFER steels during their elaboration by mechanical milling and hot isostatic pressing, *J. Nucl. Mater.* 335 (2004) 83–102. <https://doi.org/10.1016/j.jnucmat.2004.06.010>.
- [13] S. Ohtsuka, S. Ukai, M. Fujiwara, T. Kaito, T. Narita, Improvement of 9Cr-ODS martensitic steel properties by controlling excess oxygen and titanium contents, *J. Nucl. Mater.* 329-333 (2004) 372–376. <https://doi.org/10.1016/j.jnucmat.2004.04.043>.
- [14] S. Ohtsuka, S. Ukai, M. Fujiwara, T. Kaito, T. Narita, Nano-structure control in ODS martensitic steels by means of selecting titanium and oxygen contents, *J. Phys. Chem. Solids.* 66 (2005) 571–575. <https://doi.org/10.1016/j.jpics.2004.06.033>.
- [15] S. Ukai, S. Ohtsuka, Nano-mesoscopic structure control in 9Cr-ODS ferritic steels, *Energy Mater.* 2 (2007) 26–35. <https://doi.org/10.1179/174892407X210357>.
- [16] J. Fu, J.C. Brouwer, R.W.A. Hendriks, I.M. Richardson, M.J.M. Hermans, Microstructure characterisation and mechanical properties of ODS Eurofer steel subject to designed heat treatments, *Mater. Sci. Eng. A.* 770 (2020) 138568. <https://doi.org/10.1016/j.msea.2019.138568>.
- [17] X. Zhou, C. Li, L. Yu, H. Li, Y. Liu, Effects of Ti addition on microstructure and mechanical property of spark-plasma-sintered transformable 9Cr-ODS steels, *Fusion Eng. Des.* 135 (2018) 88–94. <https://doi.org/10.1016/j.fusengdes.2018.07.019>.
- [18] S. Noh, B.-K. Choi, C.-H. Han, S.H. Kang, J. Jang, Y.-H. Jeong, T.K. Kim, Effects of heat treatments on microstructures and mechanical properties of dual phase ODS steels for high temperature strength, *Nucl. Eng. Technol.* 45 (2013) 821–826. <https://doi.org/10.5516/NET.02.2013.529>.
- [19] T. Tanno, S. Ohtsuka, Y. Yano, T. Kaito, Y. Oba, M. Ohnuma, S. Koyama, K. Tanaka, Evaluation of mechanical properties and nano-meso structures of 9–11%Cr ODS steels, *J. Nucl. Mater.* 440 (2013) 568–574. <https://doi.org/10.1016/j.jnucmat.2013.04.006>.
- [20] S. Ukai, T. Kaito, S. Ohtsuka, T. Narita, M. Fujiwara, T. Kobayashi, Production and properties of nano-scale oxide dispersion strengthened (ODS) 9Cr martensitic steel claddings, *ISIJ Int.* 43 (2003) 2038–2045.

- [21] T. Narita, S. Ukai, S. Ohtsuka, M. Inoue, Effect of tungsten addition on microstructure and high temperature strength of 9CrODS ferritic steel, *J. Nucl. Mater.* 417 (2011) 158–161. <https://doi.org/10.1016/j.jnucmat.2011.01.060>.
- [22] S. Ohtsuka, S. Ukai, H. Sakasegawa, M. Fujiwara, T. Kaito, T. Narita, Nano-mesoscopic structural characterization of 9Cr-ODS martensitic steel for improving creep strength, *J. Nucl. Mater.* 367-370 (2007) 160–165. <https://doi.org/10.1016/j.jnucmat.2007.03.004>.
- [23] S. Ohtsuka, T. Kaito, T. Tanno, Y. Yano, S. Koyama, K. Tanaka, Microstructure and high-temperature strength of high Cr ODS tempered martensitic steels, *J. Nucl. Mater.* 442 (2013) S89–S94. <https://doi.org/10.1016/j.jnucmat.2013.06.010>.
- [24] E. Lucon, A. Leenaers, W. Vandermeulen, Post irradiation examination of a thermo-mechanically improved version of EUROFER ODS (SCK CEN-BLG-1028), SCK CEN, Mol, Belgium, 2006.
- [25] R. Lindau, A. Möslang, M. Schirra, P. Schlossmacher, M. Klimenkov, Mechanical and microstructural properties of a hiped RAFM ODS-steel, *J. Nucl. Mater.* 307–311, Part 1 (2002) 769–772. [https://doi.org/10.1016/S0022-3115\(02\)01045-0](https://doi.org/10.1016/S0022-3115(02)01045-0).
- [26] M.F. Doerner, W.D. Nix, A method for interpreting the data from depth-sensing indentation instruments, *J. Mater. Res.* 1 (1986) 601–609. <https://doi.org/10.1557/JMR.1986.0601>.
- [27] W.C. Oliver, G.M. Pharr, An improved technique for determining hardness and elastic modulus using load and displacement sensing indentation experiments, *J. Mater. Res.* 7 (1992) 1564–1583. <https://doi.org/10.1557/JMR.1992.1564>.
- [28] W.C. Oliver, G.M. Pharr, Measurement of hardness and elastic modulus by instrumented indentation: Advances in understanding and refinements to methodology, *J. Mater. Res.* 19 (2004) 3–20. <https://doi.org/10.1557/jmr.2004.19.1.3>.
- [29] J. Ribis, Y. de Carlan, Interfacial strained structure and orientation relationships of the nanosized oxide particles deduced from elasticity-driven morphology in oxide dispersion strengthened materials, *Acta Mater.* 60 (2012) 238–252. <https://doi.org/10.1016/j.actamat.2011.09.042>.
- [30] C. Heintze, F. Bergner, A. Ulbricht, M. Hernández-Mayoral, U. Keiderling, R. Lindau, T. Weissgärber, Microstructure of oxide dispersion strengthened Eurofer and iron–chromium alloys investigated by means of small-angle neutron scattering and transmission electron microscopy, *J. Nucl. Mater.* 416 (2011) 35–39. <https://doi.org/10.1016/j.jnucmat.2010.11.102>.
- [31] C. Heintze, F. Bergner, S. Akhmadaliev, E. Altstadt, Ion irradiation combined with nanoindentation as a screening test procedure for irradiation hardening, *J. Nucl. Mater.* 472 (2016) 196–205. <https://doi.org/10.1016/j.jnucmat.2015.07.023>.
- [32] S. Kim, S. Ohtsuka, T. Kaito, S. Yamashita, M. Inoue, T. Asayama, T. Shobu, Formation of nano-size oxide particles and  $\delta$ -ferrite at elevated temperature in 9Cr-ODS steel, *J. Nucl. Mater.* 417 (2011) 209–212. <https://doi.org/10.1016/j.jnucmat.2011.01.063>.
- [33] H. Bhadeshia, R. Honeycombe, Chapter 1 - Iron and Its Interstitial Solutions, in: H. Bhadeshia, R. Honeycombe (Eds.), *Steels Microstruct. Prop.* Fourth Ed., Butterworth-Heinemann, 2017: pp. 1–22. <http://www.sciencedirect.com/science/article/pii/B9780081002704000019>.

- [34] S. Ukai, *Microstructure and High-Temperature Strength of 9CrODS Ferritic Steel*, INTECH Open Access Publisher, 2011. [http://cdn.intechopen.com/pdfs/16710/InTech-Microstructure\\_and\\_high\\_temperature\\_strength\\_of\\_9crods\\_ferritic\\_steel.pdf](http://cdn.intechopen.com/pdfs/16710/InTech-Microstructure_and_high_temperature_strength_of_9crods_ferritic_steel.pdf) (accessed April 25, 2016).
- [35] K.D. Zilnyk, V.B. Oliveira, H.R.Z. Sandim, A. Möslang, D. Raabe, Martensitic transformation in Eurofer-97 and ODS-Eurofer steels: A comparative study, *J. Nucl. Mater.* 462 (2015) 360–367. <https://doi.org/10.1016/j.jnucmat.2014.12.112>.
- [36] N. Sallez, C. Hatzoglou, F. Delabrouille, D. Sornin, L. Chaffron, M. Blat-Yrieix, B. Radiguet, P. Pareige, P. Donnadieu, Y. Bréchet, Precipitates and boundaries interaction in ferritic ODS steels, *J. Nucl. Mater.* 472 (2016) 118–126. <https://doi.org/10.1016/j.jnucmat.2016.01.021>.
- [37] C. Heintze, F. Bergner, M. Hernández-Mayoral, Ion-irradiation-induced damage in Fe–Cr alloys characterized by nanoindentation, *J. Nucl. Mater.* 417 (2011) 980–983. <https://doi.org/10.1016/j.jnucmat.2010.12.196>.
- [38] E. Lucon, W. Vandermeulen, *Overview and Critical Assessment of the Tensile Properties of unirradiated and irradiated EUROFER97 (SCK•CEN-BLG-1042 REV.(1))*, Belgian Nuclear Research Center SCK-CEN (Belgium), 2007.
- [39] A. Chauhan, F. Bergner, A. Etienne, J. Aktaa, Y. de Carlan, C. Heintze, D. Litvinov, M. Hernandez-Mayoral, E. Oñorbe, B. Radiguet, A. Ulbricht, Microstructure characterization and strengthening mechanisms of oxide dispersion strengthened (ODS) Fe-9%Cr and Fe-14%Cr extruded bars, *J. Nucl. Mater.* 495 (2017) 6–19. <https://doi.org/10.1016/j.jnucmat.2017.07.060>.
- [40] I. Kuběna, J. Polák, T.P. Plocinski, C. Hébert, V. Škorík, T. Kruml, Microstructural stability of ODS steels in cyclic loading, *Fatigue Fract. Eng. Mater. Struct.* 38 (2015) 936–947. <https://doi.org/10.1111/ffe.12284>.
- [41] I. Hilger, F. Bergner, T. Weißgärber, Bimodal grain size distribution of nanostructured ferritic ODS Fe–Cr alloys, *J. Am. Ceram. Soc.* 98 (2015) 3576–3581. <https://doi.org/10.1111/jace.13833>.